

Markovian Properties of Velocity Increments in Boundary Layer Turbulence

Murat Tutkun

Institute for Energy Technology (IFE), Process and Fluid Flow Technology, 2007 Kjeller, Norway

University of Oslo, Department of Mathematics, Blindern, 0316 Oslo, Norway

Abstract

Markovian properties of the turbulent velocity increments in a flat plate boundary layer at $Re_\theta = 19\,100$ are investigated using hot-wire anemometry measurements of the streamwise velocity component in a wind tunnel. Increments of the longitudinal velocities at different wall-normal positions show that the flow exhibits Markovian properties when the separation between different scales, or the Markov-Einstein coherence length, is on the order of the Taylor microscale, λ . The results indicate that Markovian nature of turbulence evolves across the boundary layer showing certain characteristics pertaining to the distance to the wall. The connection between the Markovian properties of turbulent boundary layer and existence of the spectral gap is explored. Markovianity of the process is also discussed in relation to the nonlocal nonlinear versus local nonlinear transfer of energy, triadic interactions and dissipation.

Keywords: Markov theory, turbulence, boundary layer

1. Introduction

Markovian properties of the velocity increments of turbulent velocity fluctuations have recently been investigated for different flows, i.e. high Reynolds number axisymmetric turbulent jet [1, 2], high Reynolds number grid turbulence [3], cylinder wake turbulence [4], fractal-generated grid turbulence [5] and wind turbine array boundary layer [6, 7]. These studies have concluded that statistics of longitudinal velocity increments exhibit Markovian properties when scale difference (or size difference between the scales) approximately equals to the Taylor microscale, λ . This is a common observation even though the flows and Reynolds numbers of investigated cases are different [8].

One of the most difficult aspects of turbulence is existence of a wide range of scales in the flow. The large (integral) scales, which are characterized by the boundary conditions of the flow, are the scales where the turbulence kinetic energy is injected into the flow. The kinetic energy is then transferred from large scales to smaller scales through the turbulence cascade, which forms a hierarchy of scales at different sizes. At the other extreme, the smallest scales (characterized by the Kolmogorov microscale) dissipate the turbulence kinetic energy into internal energy by the action of viscosity. At very high Reynolds numbers, Kolmogorov's classical turbulence theory suggests a layer between the large, energy containing, and small, dissipative scales [9]. This layer is indeed formed by a range of scales which are independent of both extremes of the spectrum and called inertial sublayer.

All fluid motion, whether turbulent or laminar, are governed by the Navier-Stokes equation. The instantaneous, incompressible momentum equations for a Newtonian fluid reads as follows:

$$\frac{\partial \tilde{u}_i}{\partial t} + \frac{\partial \tilde{u}_i \tilde{u}_j}{\partial x_j} = -\frac{1}{\rho} \frac{\partial \tilde{p}}{\partial x_i} + \nu \frac{\partial^2 \tilde{u}_i}{\partial x_i \partial x_j} \quad (1)$$

where \tilde{u}_i and \tilde{p} denote i -th component of the instantaneous velocity and instantaneous pressure respectively. The kinematic viscosity (ν) is defined as $\nu = \mu/\rho$, where μ and ρ represent dynamic viscosity and density respectively. Instantaneous variables can be decomposed into its mean and fluctuating components using the Reynolds decomposition technique. For example, $\tilde{u}_i = U_i + u_i$, where U_i denotes the mean velocity based on ensemble averaging and u_i denotes the fluctuating component. Plugging decomposed variables into Eq. (1) and averaging yield mean momentum equations and Reynolds averaged Navier-Stokes equations.

The nature of turbulence consists of an interaction of all existing scales. This is mathematically described by the nonlinear convective term of the Navier-Stokes equation, which is the second term on left-hand-side of Eq. (1). The so-called triadic interactions of scales caused by this term is best understood when the Navier-Stokes equation is written in Fourier space. The Fourier transformation of the convective term leads to convolution and results in interaction of all scales of motion. This interaction necessitates multipoint statistics in order to obtain a complete description of the cascade. In this framework, existence of the Markovian behavior in turbulent fluctuations is shown to be useful for gaining new insight into the structure of turbulence [1, 3, 5] and the cascade of energy from large scales to small scales [10].

Statistics of the longitudinal velocity differences (or velocity increments) measured over certain physical separations in space are often studied to characterize the cascade of turbulence in physical space:

$$v(x, r) = u(x + r) - u(x) \quad (2)$$

where u and v denote velocity fluctuations and difference in u measured over r the physical separation in the streamwise direction x . Note that the Taylor's frozen field hypothesis is utilized to convert time-resolved hot-wire data to spatial data, e.g., converting $u(t)$ to $u(x)$. In a similar fashion, time separation between successive data points in time is converted to physical separation r . Eq. (2) is fundamentally important because of the fact that Kolmogorov [9] predicts the n^{th} -order structure function, $\langle [v(r)]^n \rangle$, to be a function of r and n only, i.e. $\langle [v(r)]^n \rangle \sim r^{n/3}$. Furthermore, when $n = 2$, the second order structure function, $\langle [v(r)]^2 \rangle$, quantitatively describes the distribution of turbulence kinetic energy over different scales defined by the separation r .

One way of studying the moments of velocity differences, hence the structure functions, is to calculate the probability density function (PDF) of the velocity differences at different scales, $p(v, r)$. Since a complete description of the turbulence cascade is only possible by considering the interaction of all scales of the motion, construction of the multiscale (or N -scale) joint PDF, $p(v_1, r_1; v_2, r_2; \dots; v_N, r_N)$, is necessary. (Note that the notation introduced in Ref. [1] is used here, e.g., the scale r_i is nested into the scale r_{i+1} , and N is the maximum number of different scales within the flow field.) In other words, the probability for a velocity difference occurring at a certain scale can be computed in connection with the other possible velocity differences occurring at the corresponding scales. This essentially means that any velocity difference at any scale, i.e. v_i at r_i , should be conditioned on all other differences and their corresponding scales. In this case, the conditional PDF can be defined as $p(v_1, r_1 | v_2, r_2; \dots; v_N, r_N)$, where $r_1 < r_2 < \dots < r_N$. The conditional PDF is obtained using the joint probability density functions as follows:

$$p(v_1, r_1 | v_2, r_2; \dots; v_N, r_N) = \frac{p(v_1, r_1; v_2, r_2; \dots; v_N, r_N)}{p(v_2, r_2; \dots; v_N, r_N)} \quad (3)$$

Even though the N -scale conditional PDF provides a complete description of the relationship between the velocity difference and scale relation across the cascade, in practice it is very difficult to construct this quantity because of the tremendous number of scales existing in turbulence. The difficulty of getting the N -scale statistics intensifies even more as the Reynolds number increases, since the length of the cascade and number of the scales increase with increasing Reynolds number. Application of the Markov theory,

on the other hand, can introduce a substantial simplification in the formulation of the N -scale conditional PDF [1, 2, 4, 3, 5, 8]. This is because a stochastic process, which is the longitudinal velocity difference herein, is considered Markovian if the process, or probability of the present state, can be fully determined by the most recent state. Should the process is Markovian, the N -scale conditional PDF of the velocity differences can be simplified as follows:

$$p(v_1, r_1 | v_2, r_2; \dots; v_N, r_N) = p(v_1, r_1 | v_2, r_2) \quad (4)$$

Consequently, the N -scale joint PDF of the longitudinal velocity differences can be constructed in terms of multiplication of the conditional probability density functions:

$$p(v_1, r_1; \dots; v_N, r_N) = \prod_{i=1}^{N-1} p(v_i, r_i | v_{i+1}, r_{i+1}) p(v_N, r_N) \quad (5)$$

Since application of the mathematics of Markov processes introduces a considerable simplification in the analysis of multiscale behavior of turbulence, it is of great interest to test this in wall-bounded turbulent flows. The presence of the wall in these flows affects the structure of turbulence and increases inherent complexity due to the boundary conditions imposed at the wall. In addition, viscosity plays an important role in the inner part of the flow, in particular in the vicinity of the wall. The local Reynolds number in wall-bounded flows increases with an increasing wall-normal distance and should therefore be taken into account in the analysis.

As documented in Ref. [11], turbulent boundary layers at high Reynolds numbers (i.e. $Re_\theta \sim 20\,000$) may still show residual viscous outside of the regions where it traditionally is thought be present and important. At sufficiently high Reynolds numbers a separation of scales occurs. This means that the energetic scales at the low end of the spectrum and dissipative scales at the high end of the spectrum are separated. The dissipative scales in this case can be considered as scales independent of the large energetic scales. The range where the scale separation occurs is called as an equilibrium range. In this region, the flux of turbulence kinetic energy becomes constant and equals to the dissipation. Since the local Reynolds number changes across the layers, the viscous effects delay emergence of the scale separation at wall-normal positions sufficiently away from the wall. This means that appearance of the $k^{-5/3}$ range in the one dimensional wavenumber spectrum, or the $r^{-2/3}$ range in the second-order structure function, is not possible until the viscous effects become negligible. Therefore, it is important to investigate the Markovian properties of the turbulent boundary layer in the light of these conditions.

In this paper, we study the Markovian properties of a high Reynolds number turbulent boundary at different wall-normal positions from the near-wall region to the freestream. The main purpose of this investigation is to analyze (i) the scale differences at which the theory of Markov process is applicable, and (ii) the variation of these scales in the wall-normal direction and effect of presence of solid wall. Traditionally turbulent boundary layers have been investigated by dividing the boundary layer into different sublayers from wall to the full boundary layer thickness, δ . This division is performed according to the wall-normal position in wall-units, i.e. $y^+ = yu_\tau/\nu$, where u_τ and ν denote friction velocity and viscosity, respectively. These layers are defined as the linear sublayer ($0 < y^+ \leq 3$), buffer layer ($3 < y^+ \leq 30$), mesolayer ($30 < y^+ \leq 300$), inertial sublayer ($300 < y^+ \leq 0.1\delta^+$) and outer boundary layer ($0.1\delta^+ < y^+ \leq \delta^+$) [12]. The linear sublayer and buffer layer form the so-called viscous sublayer where the viscosity is significant. Inside the mesolayer, viscous terms can be ignored in the mean momentum equation, but should be retained in the two-point equations. The inertial sublayer (or the log-layer) is nearly inviscid and the Reynolds shear stress is approximately constant. Inside the outer boundary layer, the mean convection terms are balanced

by the gradient of Reynolds shear stress. We therefore study the Markovian nature of the velocity differences in each of these layers. The paper is organized as follows: introduction to the experimental data used in this analysis, results, discussions and conclusions.

2. Experimental Setup

The database investigated in this study is a subset of the WALLTURB database of high Reynolds number turbulent boundary layer measurements performed in the large wind tunnel of Laboratoire de Mécanique de Lille (LML) in France. The freestream velocity, U_∞ , in the LML wind tunnel was 10 m s^{-1} , corresponding to Reynolds number based on momentum thickness ($Re_\theta = U_\infty \theta / \nu$) of 19 100, which was achievable in this wind tunnel because of the long test section of the facility. The measurements were taken 18 m downstream of the beginning of the test section, where the boundary layer thickness (δ) was approximately 0.30 m.

The tunnel is a closed circuit facility whose test section has dimensions of 21.6 m in length, 2 m in width and 1 m in height. Freestream velocity of the tunnel, as continuously monitored using a Furness micromanometer, can be regulated within 0.25%. In order to carry out reliable hot-wire measurements, an air/water heat exchanger is placed in the end of the return duct to keep the tunnel temperature constant within $\pm 0.3^\circ\text{C}$. A more thorough description of the LML wind tunnel with detailed flow characterization can be found in [13, 14].

The measurements analyzed here were performed using a hot-wire rake of 143 single wire probes in order to obtain both spatial and temporal information about the turbulent boundary layer, see Ref. [15] for details. Even though the rake was comprised of 143 probes, which were distributed over an array of 13 vertical combs staggered in the spanwise direction and 11 wall-normal positions from the tunnel wall to the freestream in the wall-normal direction, we only used the measurements from the first vertical comb. A careful analysis of the blockage introduced by the rake is documented by Coudert et al [16] using a set of PIV measurements with and without the hot-wire rake in place in the wind tunnel. The measurements revealed that the blockage was a potential flow disturbance, which was further verified by a complex potential model developed to simulate the effect. In addition, single- and two-point statistics computed both disturbed and undisturbed fields supported these findings. Length (l) and diameter (d) of the sensing wire of the probes were 0.5 mm and $0.25 \mu\text{m}$ respectively. These corresponded to $l^+ (= lu_\tau/\nu)$ of 11 and $d^+ (= du_\tau/\nu)$ of 0.006. The flow parameters for the wall-normal positions where the probes were located are summarized in Table 1.

The simultaneously sampled hot-wire data were recorded at 30 kHz during 6 seconds long blocks. Even though 2000 blocks of data were collected during the experiment, a smaller subset containing approximately 37 500 integral time scale is used in our analysis. (Note that more number of blocks were also tested in order to verify the statistical accuracy.) The sampling interval (Δt) in wall-units was $\Delta t^+ \approx 0.272$ in this experiment. An in-house developed multiple channel constant temperature hot-wire anemometry system operated all of the probes. The data were sampled using a fast A/D converter with a Microstar Laboratories DAP 5400 processor on-board and saved on the disk. Calibration of the probes and conversion of the hot-wire anemometry readings into the velocities were performed using an *in situ* calibration technique [17].

3. Results

The Markovian properties of the longitudinal velocity differences are studied by testing Eq. (4) at different wall-normal positions. In order to reduce the complexity of the analysis, we limit the verification to $N = 3$ in Eq. (4). Fig. 1 shows the contour lines of the conditional PDFs $p(v_1, r_1 | v_2, r_2)$ and $p(v_1, r_1 | v_2, r_2; v_3 = 0, r_3)$ for $r_1 = \lambda$, $r_2 = \ell/2$ and $r_3 = \ell$. In order to plot the PDFs in two dimensions, v_3

y^+	U (m s ⁻¹)	λ (mm)	ℓ (mm)	r_Δ (mm)	σ_L (m s ⁻¹)
10	2.94	0.64	18.7	0.10	1.41
22	4.23	0.85	36.0	0.14	1.38
50	5.02	1.28	64.4	0.17	1.21
105	5.62	1.70	95.6	0.19	1.15
222	6.22	2.21	137.4	0.21	1.13
440	6.84	2.54	173.8	0.23	1.09
890	7.52	2.81	211.1	0.25	0.99
1810	8.23	2.45	201.3	0.27	0.85
3610	9.09	1.83	166.0	0.30	0.66
5430	9.54	1.52	145.3	0.32	0.47
7240	9.91	1.15	113.8	0.33	0.23

Table 1: Flow parameters of the turbulent boundary layer at $Re_\theta = 19\,100$. Wall-normal positions of the probes are given in wall-units, $y^+ = yu_\tau/\nu$. Taylor microscale (λ) is computed in connection with the Taylor’s frozen field hypothesis: $\lambda^2 = \langle u^2(x) \rangle / \langle (\partial u / \partial x)^2 \rangle$. The integral length scale, ℓ , is computed from the auto-correlation function, $\ell = (1/\langle u^2 \rangle) \int_0^\infty \langle u(x)u(x+r) \rangle dr$. Spatial separation between two successive data points is denoted by r_Δ . Dimensionless velocity increments are found by computing σ_L , which is the square root of the large-scale ($r \rightarrow \infty$) limit of the second-order structure function, $\sigma_L = \sqrt{2\langle u^2 \rangle}$.

is conditioned on 0, the most frequent value of v_3 (i.e., 0 is the location where the PDF peaks). In order to verify the agreement, cross-sections from the contour maps of conditional PDFs in Fig. 1 were taken at $v_2 = -\sigma_L$ and $v_2 = 0$. Fig. 2 compares the cross-sections and demonstrates how closely the three-scale conditional PDF can be represented by the two-scale conditional PDF. These figures show a good agreement between two- and three-scale conditional PDFs and qualitatively satisfy Eq. (4).

The statistics of turbulence in the boundary layer very much depend on the wall-normal location. Therefore, Markovian properties of the longitudinal velocity differences across the turbulent boundary layer have been explicitly studied at additional wall-normal locations by testing Eq. (4) in a similar fashion as shown in Figs. 1 and 2 and are detailed in Table 1. In total, 11 wall-normal positions extending from $y^+ = 10$ to $y^+ = 7240$ are studied. Variations of the Markovian nature of the velocity differences across the turbulent boundary layer and effect of solid boundary, hence viscosity, on the Markovian properties are investigated as well. Fig. 3 shows the comparisons of the conditional PDFs at six different representative wall-normal positions. These positions include locations in the buffer layer ($y^+ = 22$), mesolayer ($y^+ = 105$), inertial layer ($y^+ = 440, 1810$), outer layer ($y^+ = 5430$) and edge of the turbulent boundary layer ($y^+ = \delta^+ = 7240$). Note that the physical separations in the streamwise direction used in Fig. 3 are the same as those used in Fig. 1.

Fig 3 shows that the statistics of the longitudinal velocity differences exhibit Markovian nature at all wall-normal positions, except the last position at approximately $y = \delta$, provided that $r_1 = \lambda$, $r_2 = \ell/2$ and $r_3 = \ell$. The two-scale conditional PDFs compare well with the three-scale conditional PDFs, even though the shape of the contour maps evolve with an increasing wall-normal distance. As the probe moves away from the wall through the layers, the contour maps gradually get longer along the axis representing v_1 . The contour lines along the axis representing v_2 are similar to each other from wall to the outer layer, where extension in v_1 directions are accompanied by shortening in v_2 . This essentially means that the velocity differences occurring at two different scales characterized by r_1 and r_2 become similar to each other. The size of the scales where the velocity differences are computed over, therefore, approach each other. This can be attributed to the nature of wall-bounded flows in which the largest turbulent fluctuations, hence more

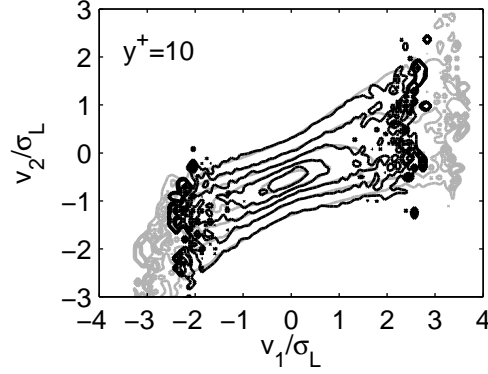


Figure 1: Verification of the Markovian nature of the velocity differences by comparing $p(v_1, r_1 | v_2, r_2)$, presented by grey contour lines, and $p(v_1, r_1 | v_2, r_2; v_3 = 0, r_3)$, presented by black contour lines. The physical separations in the streamwise direction: $r_1 = \lambda$, $r_2 = \ell/2$ and $r_3 = \ell$. The contour values: (0.2 (outermost), 0.4, 0.6, 0.8, 1.0 (innermost)).

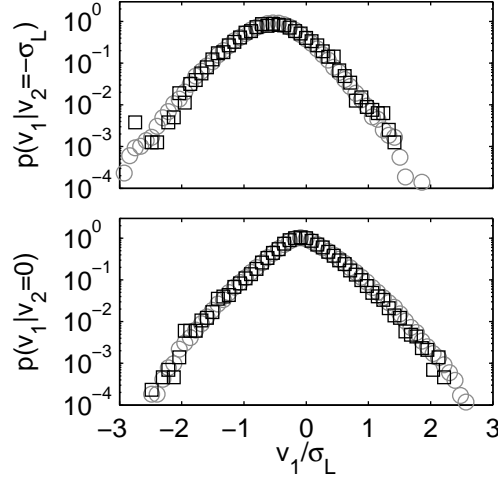


Figure 2: Cross-sections of Fig. 1 at $v_2 = -\sigma_L$ and $v_2 = \sigma_L$: \circ , $p(v_1, r_1 | v_2, r_2)$; \square , $p(v_1, r_1 | v_2, r_2; v_3 = 0, r_3)$.

variations in velocity differences, occur close to the wall.

The shape of the contour lines of the conditional PDFs at $y^+ = 5430$ ($0.75\delta^+$) changes substantially. Even though the Markovian property is still present at this wall-normal location, the collapse of the contour lines seems to be confined toward to center. At $0.75\delta^+$, entrainment, i.e. mixing the non-vortical laminar flow into the boundary layer, is a dominant flow phenomenon and modifies the structure of turbulence. This is strongly felt by the stochastic process. Close to edge of the boundary layer, a developed turbulence cascade is difficult to achieve due to the entrainment. This, therefore, leads to a less Markovian behavior. At the last measurement location, which is the edge of the boundary layer at $y^+ = \delta^+ = 7240$, the two- and three-scale conditional PDFs never collapse regardless of the size of the scales and scale differences investigated in this paper. Our observation regarding the less Markovian behavior due to the entrainment was also previously noticed in passive scalar field in a high Reynolds number grid turbulence where the internal intermittency is strong in the scalar field [3].

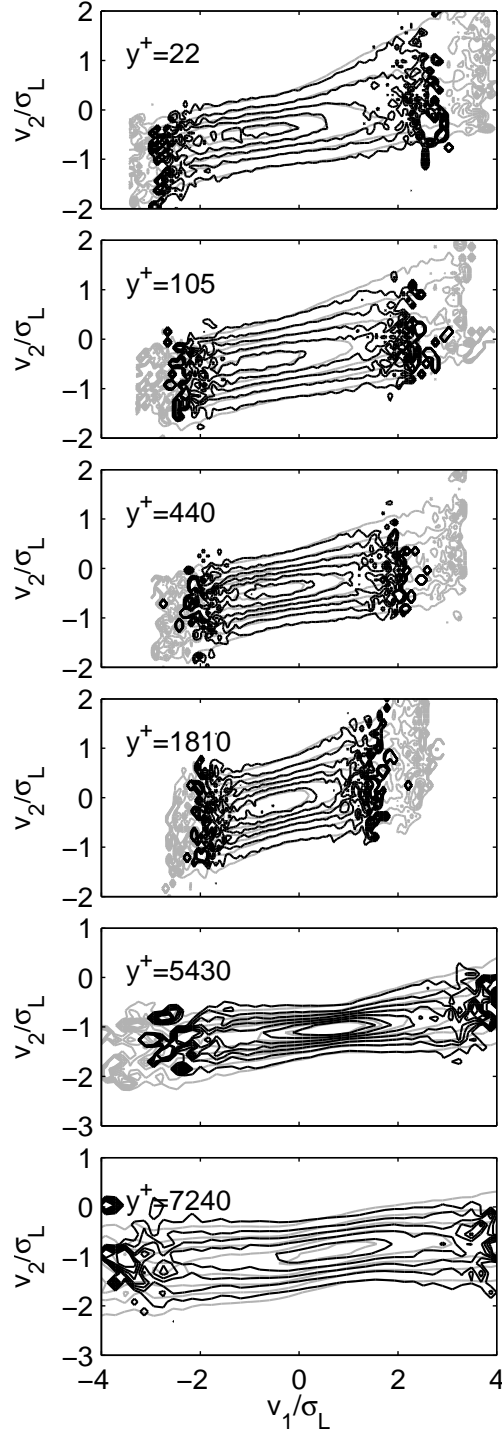


Figure 3: Verification of the Markovian nature of the velocity differences at different wall-normal positions by comparing $p(v_1, r_1 | v_2, r_2)$, presented by grey contour lines, and $p(v_1, r_1 | v_2, r_2; v_3 = 0, r_3)$, presented by black contour lines. The physical separations in the streamwise direction: $r_1 = \lambda$, $r_2 = \ell/2$ and $r_3 = \ell$. The contour values: (0.2 (outermost), 0.4, 0.6, 0.8, 1.0, 1.2 (innermost)).

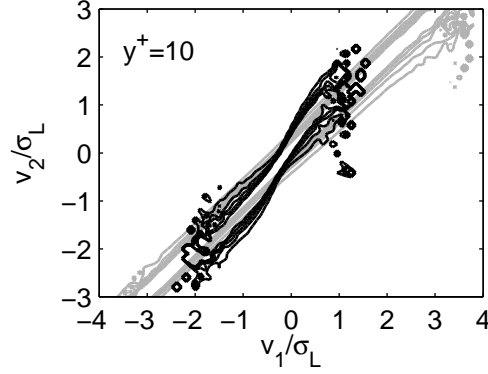


Figure 4: Disappearing Markovian nature of the velocity differences for smaller separation of the scales by comparing $p(v_1, r_1 | v_2, r_2)$, presented by grey contour lines, and $p(v_1, r_1 | v_2, r_2; v_3 = 0, r_3)$, presented by black contour lines. The physical separations in the streamwise direction: $r_1 = \ell/2 - \lambda/4$, $r_2 = \ell/2$ and $r_3 = \ell/2 + \lambda/4$. The contour values: (0.2 (outermost), 0.4, 0.6, 0.8, 1.0 (innermost)).

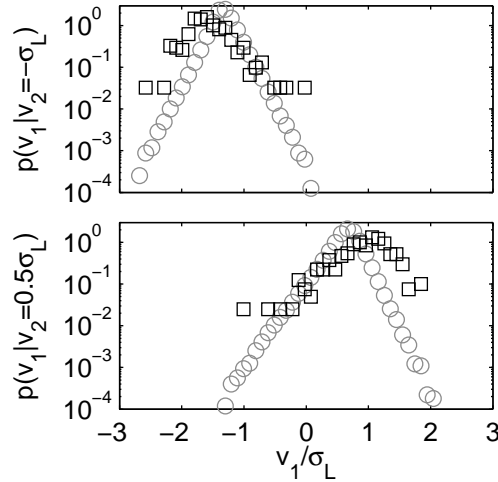


Figure 5: Cross-sections of Fig. 4 at $v_2 = -\sigma_L$ and $v_2 = \sigma_L$: \circ , $p(v_1, r_1 | v_2, r_2)$; \square , $p(v_1, r_1 | v_2, r_2; v_3 = 0, r_3)$.

Since the statistics of the longitudinal velocity differences satisfy the necessary condition for classification of the process as Markovian at certain separations, it is of great interest to find the scale differences where the Markovian property disappears. One suitable way of checking this is to compute two-scale and three-scale conditional PDFs for scale differences smaller than Taylor microscale. When the separation between the scales (Δr) is small, for example $(\Delta r) = -\lambda/4$ meaning $r_1 = \ell/2 - \lambda/4$, $r_2 = \ell/2$ and $r_3 = \ell/2 + \lambda/4$, the contour lines of the two-scale and three-scale conditional PDFs deviate from each other as shown in Fig. 4. This is further examined by comparing the cross-sections of the conditional PDFs at different v_2 values as demonstrated in Fig. 5. These two figures clearly indicate the inequality of two- and three-scale conditional PDFs, and therefore inapplicability of the Markov properties.

Even though comparing the conditional PDFs as in Fig. 4 and showing the non-overlapping contour lines are an explicit way of identifying the vanishing Markovian nature of the process, it still is very dif-

difficult to assess the level of inequality in Eq. (4). Therefore, we further investigate the dependence of the Markovian properties of the velocity differences on different scales and scale differences by studying the distribution of two sets of conditional velocity differences, denoted by x and y . These increments are created following Ref. [1]:

$$x \equiv v_1(r_1)|_{v_2(r_2)} \quad (6)$$

$$y \equiv v_1(r_1)|_{v_2(r_2), v_3(r_3)} \quad (7)$$

where the physical separation differences, Δr , between different scales, i.e. $r_3 - r_2$ and $r_2 - r_1$, are chosen to be equal to each other in order to reduce the number of parameters. The PDFs of x and y indeed yield both sides of Eq. (4). Testing the equality $p(x) = p(y)$ is the same as explicit testing of Eq. (4). One way of verifying this is to generate x and y and compare the probability density functions of x and y directly by plotting them together. However, a more quantitative measure is needed in order to assess the relation between the scales, scale differences and the Markovian nature in detail.

A non-parametric statistical test, the Wilcoxon rank-sum test (or the Mann-Whitney U-test), can be used to identify the scales and scale differences at which these two stochastic variables (x and y) have the same probability distributions [1, 8, 18]. The analysis starts with computing total number of inversions, denoted by Q , once samples of $x = [x_1, x_2, \dots, x_n]$ and $y = [y_1, y_2, \dots, y_m]$ are merged and sorted in an ascending order. For a sufficiently large sample size, i.e. $m, n > 25$ as in our case here, Q is normally distributed with a mean value $\langle Q \rangle = mn/2$ and a standard deviation $\sigma_q = (mn(m+n+1)/12)^{1/2}$, provided that the equality $p(x) = p(y)$ is satisfied. The absolute value of the standardized variable is defined as $\Delta Q = |Q - \langle Q \rangle| / \sigma_q$. This is a half-normal distributed random variable with a mean equal to $\sqrt{2/\pi}$. Dividing the standardized variable by its mean yields $\Delta Q^* = |Q - \langle Q \rangle| / (\sigma_q \sqrt{2/\pi})$. The expected value, $\langle \Delta Q^* \rangle$, is equal to 1, if the probability distribution of stochastic variables x and y become the same, i.e. $p(x) = p(y)$. Likewise, the level of departure from the expected value of 1 indicates the level of disagreement between the conditional PDFs.

In this study, $\langle Q^* \rangle$ was a function of the physical separations r_1 , r_2 and r_3 . Therefore, it was possible to visualize the dependence of the Markovian property on the size of the scales by changing the r values. Since $r_3 - r_2 = r_2 - r_1 = \Delta r$, $\langle Q^* \rangle$ is a function of only r_1 and Δr . In order to obtain a complete picture on the scales at which the longitudinal velocity differences exhibit Markovian properties, r_1 and Δr were varied within the following ranges: $1.5 \leq r_1/\lambda \leq 20$ and $0.1 \leq \Delta r/\lambda \leq 5$. These were repeated for all y^+ locations tabulated in Table 1. Note that, except for the first two probes located at $y^+ = 10$ and 22 , the hot-wire probes properly resolved turbulence scales down to 0.1λ . (The probes began rolling-off at 0.25λ at $y^+ = 10$, and 0.18λ at $y^+ = 22$.)

Fig. 6 shows the variation of $\langle Q^* \rangle$ as a function of Δr and r_1 across the boundary layer for seven different wall-normal positions, which were previously examined in Figs. 1 and 3. Even though the differences in scale separations were changed up to 5λ , the figures here are limited only to $\Delta r/\lambda = 2$. This is because no noticeable variation in the curves were observed after $\Delta r/\lambda = 1$. A straight line presenting $\langle Q^* \rangle = 1$ is also shown in order to highlight the scale differences where the equality $p(x) = p(y)$ is observed.

An immediate observation in Fig. 6 is that $\langle Q^* \rangle$ does not depend on the selection of r_1 , which essentially defines the smallest eddy size which is being taken into account. Note that r_1 should be about Taylor microscale [1, 8]. There appear some small differences in $\langle Q^* \rangle$ for different r_1 values at y^+ of 10 and 22 when $\Delta r/\lambda$ is smaller than 0.3 and 0.2 respectively. These differences are caused by the probe resolution issues as mentioned earlier experimental setup section.

Fig. 6 is useful in order to see the general trend of Markovian properties across the layers. In the near

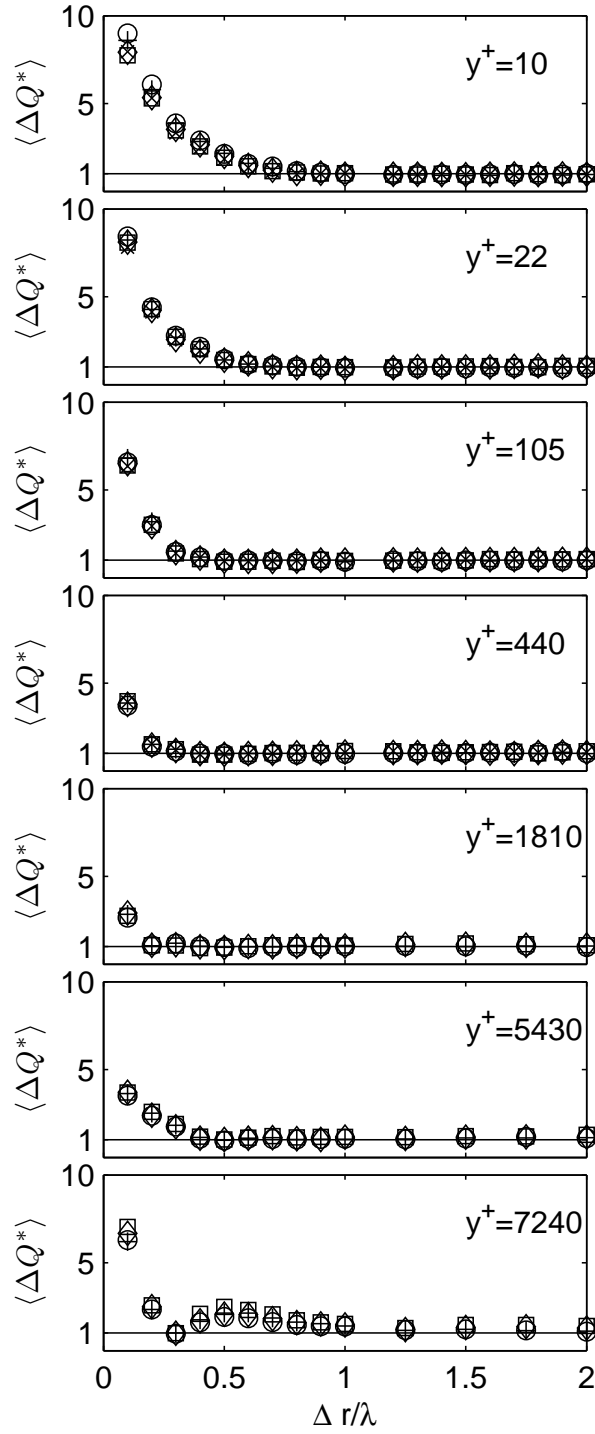


Figure 6: Behavior of $\langle \Delta Q^* \rangle$ from wall to freestream for different r_1 and Δr . ($r_3 - r_2 = r_2 - r_1 = \Delta r$) Markers denote different physical separations, r_1 : \times , 1.5λ ; \square , 2.5λ ; \diamond , 5λ ; $+$, 10λ ; \circ , 20λ . The significance level (α) is 0.05.

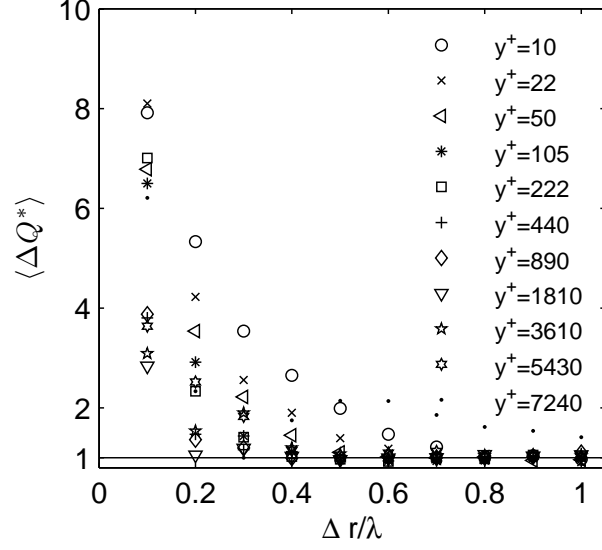


Figure 7: Close-up of the $\langle \Delta Q^* \rangle$ when $r_1 = 5\lambda$.

wall-region, y^+ of 10 and 22, values of Δr where Eq. (4) is satisfied are larger than 0.5λ . A much faster convergence of the curves onto the $\langle Q^* \rangle = 1$ is observed as the probe moves away from the wall. Finally, the $\langle Q^* \rangle$ values at $y^+ = 7240$ reveal that the statistics of the velocity differences at this wall-normal location cannot be considered as Markovian at all.

A close-up of $\langle Q^* \rangle$ versus $\Delta r / \lambda$ for all y^+ locations measured in the experiment is presented in Fig. 7 for a clear identification of the Δr values at which the process can be considered Markovian. The scale difference in this case is called Markov-Einstein coherence length [8], ℓ_{mar} , and identified as the first value of Δr where $\langle Q^* \rangle$ becomes equal to one or is within the confidence interval around one. Fig. 7 shows that there is no validation of the equality of $p(x)$ and $p(y)$ when Δr is smaller than 0.4λ . It also verifies the non-converging behavior of the $\langle Q^* \rangle$ for the last y^+ location, which has significant portion of its measurement time in the laminar external flow.

Fig. 8 compiles the scale differences at different y^+ locations for which the sufficient condition for Markov processes, Eq. (4), is satisfied. The last measurement location is not present in Fig. 8, because the statistics never exhibit Markovian nature. The accurate $\Delta r / \lambda$ values crossing the $\langle Q^* \rangle = 1$ line are identified by computing $\langle Q^* \rangle$ with very small increments in scale differences. However, one should note that these small increments are bounded by the temporal resolution (or spatial resolution in the streamwise direction in this case). In general, $\Delta r = 0.1\lambda$ was enough to determine the $\langle Q^* \rangle = 1$ crossing clearly.

The two positions in the near-wall region inside the buffer layer, $y^+ = 10$ and 22, we observe slightly higher $\Delta r / \lambda$ values compared to the rest of the boundary layer. Outside of the near-wall region, there are three distinct regions that can be identified in Fig. 8: (i) A logarithmic decay from y^+ of 50 to 222, (ii) a constant layer at $\Delta r / \lambda = 0.4$ between y^+ of 440 and 1810, and (iii) another constant layer at $\Delta r / \lambda = 0.5$ from $y^+ = 3610$ to 5430. It should be noted that the constant layer in the outer layer is based only on two measurement points and the uncertainty is considerably large. Therefore, further refinement in measured points is needed to arrive in a less uncertain conclusion. Even though the statistics of the velocity differences can be considered Markovian for values $\Delta r \sim \lambda$ or larger, which are consistent with other free shear or

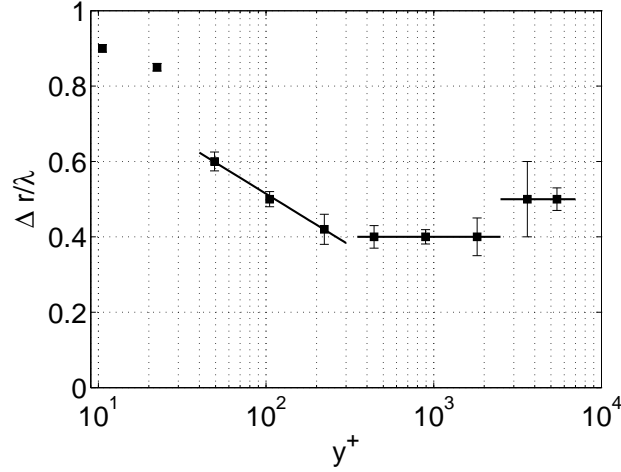


Figure 8: The smallest separation (Δr) between different scales at which longitudinal velocity difference begin exhibiting Markovian properties as a function of the wall-normal location (y^+) in the turbulent boundary layer. The best curve fit to the data between y^+ of 50 and 222 has a functional form: $\Delta r/\lambda = -0.119 \ln(y^+) + 1.0624$.

decaying turbulence flows at different Reynolds numbers [8, 3, 5], $\Delta r/\lambda$ follows different trends across the boundary layer depending on the wall-normal position.

Fig. 8 can also be studied using the sublayers of the turbulent boundary layer. The ratio of $\Delta r/\lambda$ is relatively high inside the buffer layer ($3 < y^+ < 30$) in which viscous stresses together with the Reynolds stresses act directly on the mean flow. The ratio of $\Delta r/\lambda$ decreases as the y^+ increases through the mesolayer ($30 < y^+ < 300$), in which viscosity affects all scales of motion of turbulence even though the viscous stresses become negligible [12, 19]. A constant $\Delta r/\lambda$ is observed across the log-layer ($300 < y^+ < 0.25\delta^+$), where the Reynolds shear stress is approximately constant and the viscous effects are negligible. Inside the so-called wake region extending from $0.25\delta^+$ to δ^+ , the mean flow can be treated inviscid and Fig. 8 shows constant $\Delta r/\lambda$ value of 0.5 (with a large uncertainty).

Effect of solid boundary, hence the viscosity, is substantial in the near-wall region. As the distance to the wall in the wall-normal direction increases, the viscous effects weakens. The shear is maximum in this region and creates highly anisotropic turbulent fluctuations, which can further cause longer memory, in particular in the streamwise direction. Above the buffer layer, however, the mean momentum equation can be treated inviscid. As pointed out in Ref. [12], the viscosity within the mesolayer continues to affect the turbulence at all scales ranging from the energy containing large scales to the dissipative ones, in particular in the absence of true inertial layer. As we move away from the wall, the flow shows a weaker dependence on viscosity. The decrease of $\Delta r/\lambda$ between y^+ of 30 and 300 can be attributed to the role viscosity plays. The turbulent eddies populating the log-layer have similar characteristics and therefore lead a constant separation length. In the outer layer, the effect of entrainment becomes important, hence the $\Delta r/\lambda$ values observed in this region are indeed similar to the ones observed in grid turbulence [3] and cylinder wake turbulence [8].

4. Premultiplied spectra

In light of above discussions, it is useful to check the turbulence spectra in particular inside the log-layer. Fig. 9 shows the premultiplied one-dimensional wave number spectra $k_1^{5/3} F_{1,1}(k_1)$ at three different

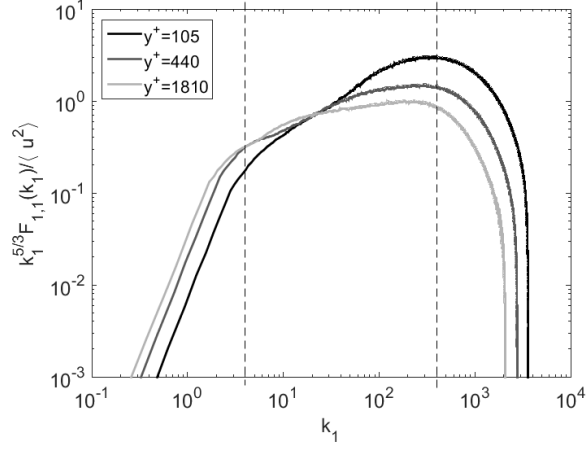


Figure 9: Premultiplied spectra, $k_1^{5/3} F_{1,1}(k_1) / \langle u^2 \rangle$, at y^+ of 105, 440 and 1810. Dashed lines indicate the region enclosed by $k_1 = 4$ and $k_1 = 400$.

wall-normal positions, i.e. $y^+ = 105$ (mesolayer), $y^+ = 440$ (beginning of log-layer) and $y^+ = 1810$ (end of log-layer). The one dimensional spectra are also normalized by the local variance, $\langle u^2 \rangle$. Since the one-dimensional wave number spectra are premultiplied by $k_1^{5/3}$, the true log-layer (or the inertial sublayer) should be flat and parallel to the abscissa. If existed, the flat region, or the so-called spectral gap, indicates a separation of energy-containing and dissipative scales of turbulence. However, the flat region in each of these premultiplied spectra presented in Fig. 9 is extremely small, even though our turbulent boundary layer is indeed a high Reynolds number flow ($Re_\theta = 19\,100$). The premultiplied spectra, on the other hand, display a development toward a wide flat region. We observe that slopes of the premultiplied spectra decrease in a region between k_1 of 4 and 400, as the local Reynolds number (or y^+) increases. Even the top of log-layer at (y^+) of 1810, on the other hand, do not have scale-separation, or constant flux regions. This further means that transfer of energy in the absence of scale separation occurs non-locally.

Fig 10 is produced by integrating the one-dimensional wave number spectra presented in Fig. 9 over the wave number space. The solid and dashed lines show the energy and dissipation spectra at three different wall-normal positions, respectively. As clearly shown, there exists no spectra gap between the energy and dissipation spectra. Dissipation already starts at quite low wavenumbers corresponding to scales which are considered energetic. As we move away from the wall, the overlap between the energy and dissipation spectra reduces, however, it is always finite even at the top of the log-layer. Similar results were previously documented by George and Tutkun [20] for a wider range of wall-normal positions.

5. Summary and Conclusion

In this paper, it has been shown that the statistics of the longitudinal velocity differences in a high Reynolds number ($Re_\theta = 19\,100$) boundary layer turbulence have Markovian properties similar to those documented in other flows[1, 2, 3, 4, 5, 8]. Our study differs from the previous studies which were free shear flows far from solid boundaries, and therefore the Reynolds stress equation was inviscid. Equality of the three-scale conditional PDFs to the two-scale conditional PDFs is tested across the turbulent boundary layer and Markovian properties are observed for $\Delta r \gtrsim \lambda$ at all measurement locations considered here, except at $y \sim \delta$.

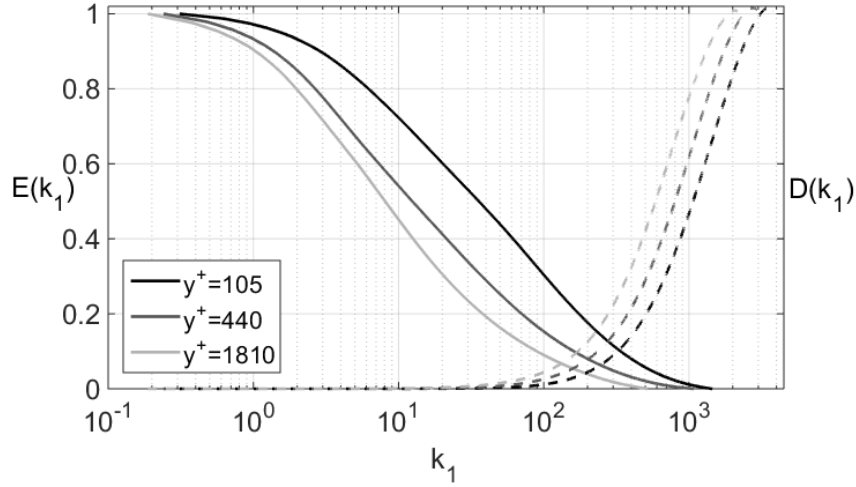


Figure 10: Solid lines represent running integrals of one-dimensional wave number spectra normalized by turbulence kinetic energy, $\langle u^2 \rangle$: $E(k_1) = 1 - \frac{1}{\langle u^2 \rangle} \int_0^{k_1} F_{11}(k) dk$. Dashed lines represent running integrals of dissipation spectra normalized by dissipation, ϵ : $D(k_1) = \frac{15\nu}{\epsilon} \int_0^{k_1} k^2 F_{11}(k) dk$.

As a non-parametric statistical test, the Wilcoxon rank-sum test is used in order to quantify the level of agreement (or disagreement) between the two- and three-scale conditional PDFs. Experimental utilization of the Wilcoxon test reveals that the smallest scale difference, expressed in terms of Taylor microscale, at which the statistics of the velocity differences begin exhibiting the Markovian nature varies across the boundary layer. In the viscosity dominated buffer layer, the largest $\Delta r/\lambda$ is needed for the emergence of Markovian behavior as compared to rest of the boundary layer. This is mainly attributed to the boundary conditions imposed by the solid wall, dominance of the viscosity therein and the local Reynolds number. As the turbulent eddies are elongated in the streamwise direction due to presence of large shear in this region, the memory effects are expected to be slightly longer in the streamwise direction. In addition, the larger eddies of the turbulent boundary layer modulates the smaller eddies near the wall, and this enhances the memory of the process. Therefore, larger physical separations between the scales are needed in the near-wall region in order to satisfy the equality of two- and three-scale conditional PDFs.

Across the mesolayer, a logarithmic decay of $\Delta r/\lambda$ is observed with an increasing y^+ . It appears that as the influence of viscosity on turbulence quantities gradually becomes negligible [12, 19], the scale difference needed for Markovian properties shortens through the mesolayer. After the logarithmically decreasing trend, a constant value of $\Delta r/\lambda = 0.4$ is present through the inertial sublayer (or the log-layer). This means that the memory effects between the scales of motion in this region are approximately the same regardless of wall-normal position. Entrainment in the outer layer increases the uncertainty level and causes larger $\Delta r/\lambda$ values than the ones observed in the log-layer. Here $\Delta r/\lambda$ becomes 0.5 with noticeable uncertainty. The last measurement position on the edge of turbulent boundary layer never shows Markovian behavior which is attributed to the strongly intermittent flow because of entrainment and absence of a turbulence cascade at this location.

The convective term in the Navier-Stokes equations is responsible for nonlinear interactions and transfer of kinetic energy across different eddies of turbulence. Fourier transformation of the Navier-Stokes equation

leads to convolution of the convective term and further reveals that the nonlinear interactions in spectral space are third order. This means that the wavenumbers representing different scales of motion in real space form triads in spectral space. The triad may result in a nonlocal transfer of energy between the eddies in certain situations. Formation of the triad needs interaction of three wavenumbers, e.g., $\vec{k}_l + \vec{k}_{d1} = \vec{k}_{d2}$, representing two very large (corresponding to dissipative scales) wavenumbers \vec{k}_{d1} and \vec{k}_{d2} and one very small (corresponding to energetic large scales) wavenumbers, \vec{k}_l . Once the triadic interaction exists, the large and small wavenumbers interact. The nonlocal transfer of energy through the interaction of large and small scales relates to the memory in the cascade process. Kolmogorov's classical theory for turbulence suggests that the nonlinear transfer of energy at very large Reynolds numbers with a clear separation of scales occurs only locally inside the inertial subrange [9]. Even though the inertial sublayer can be described as a complete Markovian process at very high Reynolds numbers, this can never be achieved for dissipative scales, first due to the dissipation and second due to triadic interactions.

Breakdown of the Markovian property indicates the interaction of well-separated scales, hence existence of the nonlocal nonlinear interactions. Our investigation on the high Reynolds number turbulent boundary layer suggests that non-Markovian behavior is possible at scale differences smaller than Taylor microscale. As studied herein, extent and strength of the process memory can be characterized by the $\langle Q^* \rangle$ value. The greater departures from $\langle Q^* \rangle = 1$ indicate shorter memory, hence more local nonlinear interactions. This essentially in agreement with the recent findings of Ref. [11], in which it was shown that departures from the Kolmogorov's $k^{-5/3}$ range in the turbulence spectra always existed in turbulent boundary layers even at high Reynolds numbers. Previously, similar results, i.e. departures from the true $k^{-5/3}$, were observed in a high Reynolds number grid turbulence [21].

An investigation by Carlier et al. [22] on the local nonlinear and nonlocal nonlinear transfer of energy in a turbulent boundary layer at $Re_\theta = 20\,600$ demonstrated the dominance of local nonlinear interactions in the energy-containing, low wavenumber part of the spectrum. They also showed the dominance of nonlocal nonlinear interactions in the dissipative, high wavenumber part of the spectrum. Even at $Re_\theta = 20\,600$, significant nonlocal nonlinear interactions, in particular in the dissipative range, indicate the absence of the separation of scales. In a computational study, Laval [23] showed that it was possible to improve the departure from Kolmogorov's ($k^{-5/3}$) range once the nonlocal nonlinear interactions were suppressed during the computation.

Existence of the inertial sublayer requires constant flux of turbulence kinetic energy. The flux of turbulence kinetic energy between the scales in the inertial layer should also be equal to the dissipation [9]. Refs. [24, 25, 26] show that most of the flux in the inertial sublayer is indeed due to local nonlinear interactions. However, nonlocal interactions were found to be accounting for $\sim 20\%$ of the total flux of energy across the inertial sublayer. This causes the slope of premultiplied spectra within the inertial range in Fig. 9 to be finite, never achieving null value. On the other hand, nonlocal nonlinear interactions become dominant in the dissipative range of the turbulence spectrum [24, 25, 26], supporting previous studies of Carlier et al [22] and Laval [23]. Also noted in Refs. [24, 25, 26] is the scaling of nonlinear energy flux with the Reynolds number. It seems that as the Reynolds number increases, the nonlinear interactions weaken and there is a convergence toward the Kolmogorov's high Reynolds number turbulence description [9].

In summary, the high Reynolds number turbulent boundary layer studied here reveals that Δr , where the Markovian nature of the stochastic process emerges, always have finite values throughout the boundary layer. The local Reynolds number increases with an increasing wall-normal distance, and level of Markovianity is slightly different in different sections of the boundary layer. Should there existed a true inertial layer in our flow, which would further indicate a negligible nonlocal interactions across the inertial sublayer, it would perhaps be possible to see $\Delta r/\lambda$ converging to null, at least in the log-layer. In this case, a

complete Markovian description of the inertial sublayer could be obtained. This, however, in a real-world turbulent flow is not possible because of the fact that it would need null dissipation as well. Even though most dissipation happens at the higher end of the spectrum, it is always finite across the cascade, and will eventually destroy the complete Markovian description. Kolmogorov [9] predicts that the transfer of turbulence kinetic energy occurs only locally through the local nonlinear interactions when there exist an inertial subrange, which is a very high Reynolds number property. As long as the energy exchange between the scales is a nonlinear process, triadic interactions present and prevents $\Delta r/\lambda$ converging to null. According to George and Castillo [12], the Reynolds number should be about $Re_\theta \gg 10\,000$ for turbulent boundary layers for emergence of a true spectral gap. This means that turbulent boundary layer experiments at much higher Reynolds numbers than the one tested in this study are needed to further explore the relation between Markovian nature of the flow and its relation to spectral gap across the energy spectrum.

Acknowledgements

The author would like to thank Maren Fredbo for her involvement in the early stage of the work and Elizabeth H. Camp for her careful revision and useful discussions. A partial financial support was provided by the research project DOMT funded by the Research Council of Norway with project number 231491 under the FRINATEK program.

- [1] C. Renner, J. Peinke, R. Friedrich, Experimental indications for markov properties of small-scale turbulence, *J. Fluid Mech.* 433 (2001) 383.
- [2] C. Renner, J. Peinke, R. Friedrich, O. Chanal, B. Chabaud, Universality of small-scale turbulence, *Phys. Rev. Lett.* 89 (2002) 124502.
- [3] M. Tutkun, L. Mydlarski, Markovian properties of passive scalar increments in grid-generated turbulence, *New J. Phys.* 6 (49) (2004) 1–24.
- [4] M. Siefert, J. Peinke, Joint multi-scale statistics of longitudinal and transversal increments in small-scale wake turbulence, *J. Turbulence* 7 (50) (2006) 1–35.
- [5] R. Stresing, J. Peinke, R. E. Seoud, J. C. Vassilicos, Defining a new class of turbulent flows, *Phys. Rev. Lett.* 104 (19).
- [6] M. S. Melius, M. Tutkun, R. B. Cal, Identification of Markov process within a wind turbine array boundary layer, *Journal of Renewable and Sustainable Energy* 6 (2014) 023121.
- [7] M. S. Melius, M. Tutkun, R. B. Cal, Solution of the Fokker–Planck equation in a wind turbine array boundary layer, *Physica D: Nonlinear Phenomena* 280 (2014) 14–21.
- [8] S. Lück, C. Renner, J. Peinke, R. Friedrich, The Markov-Einstein coherence length – a new meaning for the Taylor length in turbulence, *Phys. Lett. A* 359 (2006) 335–338.
- [9] A. N. Kolmogorov, The local structure of turbulence in incompressible viscous fluid for very large reynolds numbers, *Dokl. Akad. Nauk. SSSR* 30 (1941) 301.
- [10] R. Friedrich, J. Peinke, Statistical properties of a turbulent cascade, *Physica D* 102 (1997) 147.
- [11] W. K. George, M. Tutkun, Mind the gap: a guideline for large eddy simulation, *Phil. Trans. R. Soc. A* 367 (1899) (2009) 2839–2847.
- [12] W. K. George, L. Castillo, Zero-pressure-gradient turbulent boundary layer, *Applied Mechanics Reviews* 50 (12) (1997) 689–729.
- [13] J. Carlier, M. Stanislas, Experimental study of eddy structures in a turbulent boundary layer using particle image velocimetry, *J. Fluid Mech.* 535 (2005) 143–188.
- [14] M. Stanislas, L. Perret, J.-M. Foucaut, Vortical structures in the turbulent boundary layer: a possible route to a universal representation, *J. Fluid Mech.* 602 (2008) 327–382.
- [15] M. Tutkun, W. K. George, J. Delville, M. Stanislas, P. Johansson, J.-M. Foucaut, S. Coudert, Two-point correlations in high Reynolds number flat plate turbulent boundary layers, *J. Turbulence* 10 (N21) (2009) 1–23.
- [16] S. Coudert, J.-M. Foucaut, J. Kostas, M. Stanislas, P. Braud, C. Fourment, J. Delville, M. Tutkun, F. Mehdi, P. Johansson, W. K. George, Double large field stereoscopic PIV in a high Reynolds number turbulent boundary layer, *Experiments in Fluids* 50 (1) (2011) 1–12.
- [17] M. Tutkun, W. K. George, J. M. Foucaut, S. Coudert, M. Stanislas, J. Delville, In situ calibration of hot wire probes in turbulent flows, *Exp. Fluids* 46 (4) (2009) 617–629.
- [18] R. Stresing, J. Peinke, Towards a stochastic multi-point description of turbulence, *New J. Physics* 12 (103046).

- [19] M. Wosnik, L. Castillo, W. K. George, A theory for turbulent pipe and channel flows, *J. Fluid Mech.* 421 (2000) 115–145.
- [20] W. K. George, M. Tutkun, The mesolayer and reynolds number dependencies of boundary layer turbulence, in: *Progress in Wall Turbulence: Understanding and Modeling*, Springer, 2011, pp. 183–190.
- [21] L. Mydlarski, Z. Warhaft, On the onset of high-Reynolds-number grid-generated wind tunnel turbulence, *J. Fluid Mech.* 320 (1996) 331–368.
- [22] J. Carlier, J. P. Laval, M. Stanislas, Some experimental support at a high Reynolds number to a new hypothesis for turbulence modeling, *Compt. Rend. de l'Academ. des Sci. - Ser. II B - Mech.* 329 (2001) 35–40.
- [23] J. P. Laval, B. Dubrulle, S. Nazarenko, Nonlocality and intermittency in three-dimensional turbulence, *Phy. Fluids* 13 (7) (2001) 1995–2012.
- [24] A. Alexakis, P. D. Mininni, A. Pouquet, Imprint of large-scale flows on turbulence, *Phys. Rev. Lett.* 95 (264503).
- [25] A. Alexakis, P. D. Mininni, A. Pouquet, Large scale flow effects, energy transfer, and self-similarity on turbulence, *Phys. Rev. E* 74 (056320).
- [26] A. Alexakis, P. D. Mininni, A. Pouquet, Non-local interactions in hydrodynamic turbulence at high Reynolds numbers: the slow emergence of scaling laws, *Phys. Rev. E* 77 (036306).